Suppression of vortex shedding behind a circular cylinder by another control cylinder at low Reynolds numbers

By Srikanth B. Talla, T. K. Sengupta & A. Dipankar
Department of Aerospace Engineering
I. I. T. Kanpur 208 016
INDIA

(Received 25 August 2005)

Vortex shedding behind a cylinder can be controlled by placing another control cylinder has been demonstrated experimentally by Strykowski & Sreenivasan (1990) at low Reynolds numbers. However, there are no definitive computational and theoretical studies that have explored the physical mechanism behind the phenomenon. This has not been possible mainly due to the absence of methods that can compute flows accurately past multiply connected bodies. In the present work, using an over-set grid method we report numerical results for flow past a pair of cylinders used in Strykowski & Sreenivasan (1990). Apart from providing accurate solution of Navier- Stokes equation, we also use an energy based receptivity analysis method of Sengupta et al. (2003) to focus some aspects of the physical mechanism behind vortex shedding and its control. These results are compared with the flow picture developed using a dynamical system approach based on proper orthogonal decomposition (POD) technique.

1. Introduction

Alteration of vortex shedding behind circular cylinder at low Reynolds numbers have been reported in Strykowski (1986) and Strykowski & Sreenivasan (1990) by the placement of another smaller cylinder in the near wake of the main cylinder. Mainly from experimental observations, the authors concluded that the control cylinder (i) reduces temporal growth rate of disturbances; (ii) alters or controls vortex shedding that shows up in reduced drag and removal of peak from the spectrum; (iii) changes the local stability by smearing and diffusing concentrated vorticity by diverting small amount of fluid in the near wake of the main cylinder. Vortex shedding was suppressed for Reynolds number (Re, defined by the diameter D of the main cylinder and oncoming free stream speed) below 80. They also reported numerical results for $Re = 55$ in a small physical domain ($-3.4 < x/D < 9.7$) using a second order finite difference Galerkin method. The problem was solved using a single grid and the control cylinder was modeled enforcing no-slip condition on six grid points occupying an area similar to the control cylinder.

Despite the simple flow configuration, there have been no other numerical efforts that has reproduced the experimental observations of Strykowski (1986) and Strykowski & Sreenivasan (1990). First and foremost, to study this flow one needs accurate numerical methods that is free of spurious numerical dispersion effects. It is easy to compute flows showing alternate shedding of vortices behind circular cylinder by even low- order methods that are spuriously dispersive. Also, the larger numerical error of low-order methods are in general asymmetric and hence they trigger flow asymmetry earlier. In contrast, higher order methods display onset of flow asymmetry much later (see Nair & Sengupta (1996)) due to lower level of asymmetric-error. In general, it is also seen that higher order accuracy reduces spurious dispersion effects. Additionally, low-order central schemes can be non- dissipative, but they attenuate signals due to poor implicit filtering property of the methods. Thus, it is seen that satisfaction of physical dispersion relation- termed dispersion relation preservation (DRP) property is central to computing physically unstable flows. Issues of accuracy, DRP property and numerical stability for direct numerical simulation (DNS) of transitional and turbulent flows are discussed in Sengupta (2004), which and Sengupta et al. (2003a) introduced some high accuracy compact schemes those satisfy strict requirements of DNS. Secondly, it is difficult to produce accurate solution for multiply-connected domain using structured non-orthogonal grids, as non-orthogonality introduces additional large sources of error. Solving Navier-Stokes equation using unstructured grid, as in finite element and finite volume methods, for multiply -connected domain have not been successful due to their inability to satisfy DRP property. Although these methods cite their ability to handle complex geometry as one of their advantages. This type of problem can be avoided by solving Navier-Stokes equation on a over-set orthogonal grids by high resolution DRP schemes- as used here. The requirements for DNS of physically unstable flows have been discussed in Appendix-A, where we compare the present numerical method with a traditional low order method in propagating a wave packet.

The power of the emerging DNS methodologies have not been successfully translated to compute physically unstable flows in a multiply-connected domain. Although, significant progress have been made in solving engineering problems using over-set grids for complex geometries. Developments in over-set grid method are given in Stegger & Benek (1987), Chesshire & Henshaw (1990) and Henshaw (1994). Extension of high accuracy methods in conjunction with over-set grid method is used here in solving the control of vortex shedding problem.

In reporting the results in Strykowski & Sreenivasan (1990) and Strykowski (1986), the authors identified vortex shedding due to absolute instability in the near wake due to the temporal growth of unstable modes. Jackson (1987) identified Hopf bifurcation of steady flow to produce periodic flows- even though the former may not exist physically. Sengupta et al. (2003b) have proposed vortex shedding phenomenon to arise as a temporal instability of any equilibrium solution. Theoretical explanation was based upon the time evolution of disturbance energy (E_d), which is governed by (Sengupta et al. (2003) and Sengupta et al. (2003b)),

$$\nabla^2 E_d = 2\omega_m.\omega_d + \omega_d.\omega_d - V_m.\nabla \times \omega_d - V_d.\nabla \times \omega_m - V_d.\nabla \times \omega_d. \qquad (1.1)$$

In this equation V and ω represent velocity and vorticity fields respectively. The subscripts m and d refer to mean and disturbance quantities. At any instant of time, one can solve the above Poisson equation to obtain the distribution of E_d. Thus, the evolution of E_d can be traced over the full domain by solving equation (1.1) over successive time steps. But, in Sengupta et al. (2003) and Sengupta et al. (2003b), this approach was not followed and instead the growth of E_d is predicted by looking at the presence of disturbance energy sources and sinks in the domain. It is noted that disturbance energy grows at those points where the right hand side of equation (1.1) becomes negative implying an energy source there. This generic mechanism of forecasting growth of disturbance energy is based on the full Navier-Stokes equation without any simplifying assumptions- unlike other instability theories.

Vortex shedding behind a bluff body displays complicated spatio-temporal variations that can be analyzed using POD as a tool. POD as a statistical technique, allows presenting coherent structures as a low-dimensional description of the flow. Also, POD as a linear operation allows studying the flow locally that can be used to discriminate between pockets of convective and absolute instability in bluff body flows. Deane & Mavriplis (1994) and Deane et al. (1991) have used POD technique to propose vortex shedding as due to interaction between pairs of eigen-modes that are roughly ninety degrees phase apart.

In the present study, we have tried to interpret vortex shedding and its "suppression" in terms of unsteady disturbance energy growth, as given by equation (1.1), and in terms of POD modes and their time variation. In the next section, the numerical simulation methods and results are given for the two specific cases studied. In section 3, vortex shedding is viewed in terms of unsteady disturbance growth. This is followed by characterizing vortex shedding and its control by POD in section 4. The paper closes with a summary of the present work.

2. Numerical Simulation of Vortex-shedding and Suppression Cases

In the present computations, the Navier-Stokes equation is solved in stream function-vorticity formulation. Governing equations are solved using the over- set grids shown in figure 1. Details of basic numerical methods used are given in Appendix- A. The control cylinder is positioned at $x/D = 1.75$ and $y/D = 1$ with respect to the center of the main cylinder. Two cases reported here are for $Re = 80$ and $Re = 150$- with the former displaying "suppression" of shedding while the latter displays regular periodic shed vortices in the wake. In the sub-domain Ω_1- extending up to $40D$, a (301×400)-grid has been used with 301 uniformly distributed points in the azimuthal direction. In the radial direction, the grid spacing increases by a constant amount with the wall resolution equal to $0.005D$. In the sub-domain Ω_2- extending up to $1D$, a (201×80)-grid has been used with similar grid arrangement i.e. in the azimuthal direction an equi-angular grid is used and a grid distributed in arithmetic progression in the radial direction. Here the vorticity transport equation and the stream function equation that have been solved are given by,

$$\frac{\partial \omega}{\partial t} + (V.\nabla)\omega = \frac{1}{Re}\nabla^2\omega, \tag{2.1}$$

$$\nabla^2\psi = -\omega. \tag{2.2}$$

The nondimensionalized equations have been obtained with D as the length scale and U_∞ as the velocity scale. The equations are solved subject to no-slip boundary condition on the cylinder walls and uniform flow on the inflow of Ω_1. At the outflow boundary of Ω_1, a convective boundary condition is used for (2.2): $\frac{\partial V_r}{\partial t} + V_c\frac{\partial V_r}{\partial r} = 0$, where V_r is the radial component of velocity and V_c is the convection speed calculated from the previous time step data at the outflow for V_r. This boundary condition allows smooth passage of vortices through the outflow without any spurious reflections.

Here, equations (2.1) and (2.2) are solved in each of the sub-domains (Ω_1, Ω_2) independently using synthesized boundary conditions obtained at the sub-domain boundaries. Thus, to solve the problem in Ω_1, auxiliary boundary conditions are obtained on $ABCD$ from the solution obtained in Ω_2. Similarly, to solve the problem in Ω_2, auxiliary boundary conditions are required on $PQRS$ that is supplied from the solution in Ω_1. The success of over-set grid method depends on how accurately these auxiliary boundary conditions are obtained at the inter-grid boundaries from the donor neighboring grids. The basic procedure followed in interpolating boundary data at a acceptor point (P) is to consider a cloud of donor points in its neighborhood. The interpolation of functions at these cloud of points in terms of the function and derivatives at P creates the residue given at the i^{th} point by

$$R_i = -f_i + f_P + f_x|_P \Delta x_i + f_y|_P \Delta y_i + f_{xx}|_P \frac{\Delta x_i^2}{2} + f_{yy}|_P \frac{\Delta y_i^2}{2} + f_{xy}|_P \Delta x_i \Delta y_i + ...$$

One can construct an objective function $F = \sum_{i=1}^{N} R_i^2$ and minimize it with respect to f_P and the derivatives $f_x|_P$, $f_y|_P$ etc. This shows that one requires a minimum of three donor points for linear interpolation and six donor points for quadratic interpolation. While more number of donor points can be used in a least square sense, it is note that the accuracy is degraded with large number of donor points. In the present work we have used a cloud of seven donor points for least square quadratic interpolation at all the inter-grid boundary data.

The loads are calculated for the main cylinder by solving the pressure Poisson equation (PPE) in a part of Ω_1, as given below,

$$\nabla^2(\frac{p}{\rho} + \frac{V^2}{2}) = \nabla \cdot (\vec{V} \times \vec{\omega}) \tag{2.3}$$

The quantity within the parenthesis on the left hand side is the total pressure and is a good measure to total mechanical energy for the incompressible flow under consideration. PPE is solved subject to the boundary condition derived from the normal momentum equation as applied on the solid body in Ω_1 and on the outer boundary used. It is noted that this boundary conditions are exact if the derivatives in the normal momentum equation are calculated correctly. Due to this reason, one can truncate Ω_1 for solving PPE and solve loads for different parts of multiply-connected domain separately. The rationale and procedures for solving PPE in a truncated domain can be obtained from Sengupta *et al.* (2005a). Obtained pressure and vorticity fields can be integrated to calculate the loads and moment acting on the main cylinder.

These results are shown for both the Reynolds number cases in figure 2. For $Re = 80$, plotted C_l and C_d do not show periodic variations that occur due to periodically shed vortices. However, for $Re = 150$ one can observe these periodic variations. Periodic shedding of vortices can be viewed clearly in vorticity contour plots are shown in figures 6 and 7.

3. Vortex Shedding as Unsteady Growth of Disturbances

Although equation (1.1) was developed in Sengupta *et al.* (2003) to explain sub-critical transition for a zero pressure gradient shear layer, the equation is not restricted to any flow types. In Sengupta & Dipankar (2005), the same equation and method has been used to explain the sub-critical instability of the attachment line boundary layer that is also known as the leading edge contamination problem. One of the most attractive feature of equation (1.1) is in its origin from Navier- Stokes equation sans any approximations, making it an ideal tool to study unsteady disturbance energy growth for any fluid flow. It is with this modest goal, the same equation is used here to study vortex shedding and its delay.

The advantage of equation (1.1) is its construct that allows study of disturbance energy growth with respect to any identified equilibrium state. This also makes such a study non-unique. In the present context, this has been circumvented by taking a long time average of the unsteady flow field as the equilibrium state. This is done with a view to interpret and compare POD modes (that are obtained for fluctuations with respect to long time average) with disturbance energy growth.

From figure 2, it is apparent that the flow displays periodic vortex shedding for $Re = 150$, while it is "suppressed" for $Re = 80$ with the help of the control cylinder in place in the near wake. For both the cases, the mean flow is obtained by constructing time average of the data from $t = 0$ to 49. As in Sengupta *et al.* (2003) and Sengupta & Dipankar (2005), equation (1.1) is not solved over the computational domain, instead the properties of Poisson equation is utilized to identify the energy source(s) and sink(s) as described in the introduction, by looking at the sign and magnitude of the right hand side of the equation.

In figure 3, the contours of right hand side of (1.1) is plotted at the indicated times for $Re = 150$ case. The negative contours are shown by dotted lines in all the figures. The drawn figures are over a period from $t = 31$ to 37. For an uncontrolled case, a positive vortex develops on the lower side of the cylinder (the flow being from right to left in all the figures) and a negative vortex is seen to form on the top of the cylinder. Figure 3 shows the creation of additional disturbance sources and sinks by the control cylinder that deflects the main wake- a fact identified already in Strykowski & Sreenivasan (1990). This can be readily verified from the vorticity contour plots of figure 6 for this case. Over the full cycle, the presence of energy sink on the bottom side of the control cylinder indicates significant alteration of shedding property. It is to be noted that the oncoming flow over the control cylinder is with significant shear that wraps around it in alternate sign layers. This is clearly visible at all times and the strength of the disturbances around the control cylinder is few orders of magnitude higher than that for the main cylinder. Such wrap-around disturbance sources and sinks can also work in tandem with the disturbance energy emanating from the main cylinder- as seen at $t = 35$ and 37.

In figure 4, the contours of right hand side of (1.1) is plotted for the $Re = 80$ case. Once again the oncoming flow with shear creates a wrap-around alternate layers of disturbance energy over the control cylinder. However, because of the lower Reynolds number of the flow- the interaction between the disturbance energy fields is not seen visually, except at $t = 4$. As time progresses, the disturbance energy decreases with time up to $t = 12$ and subsequently it increases slowly to its long-time behavior pattern, as shown typically at $t = 40$, when weak shedding pattern is established. It is also noted that the disturbance energy contours are relatively stronger over the main cylinder as compared to the control cylinder by an order of magnitude for this case. The overall disturbance energy levels are significantly lower for both the cylinders in figure 4, implying that the control quenches unsteadiness originating from both the cylinders. It is seen that the disturbance energy variations occur over smaller and smaller region of the flow field at later times. This is different from the case of figure 3 where both the cylinders produce significant unsteady effects and affect each other. One of the main reasons, for the difference between the two cases of $Re = 80$ and $Re = 150$ is due to the difference of the equivalent Reynolds number for the control cylinder. Considering the diameter of the control cylinder to be $1/7^{th}$ of the main cylinder, this increases the Reynolds number from 11.4 to 21.4 between the two cases. Additionally, the oncoming flow with shear will have significantly different effects at these relatively lower Reynolds numbers. The information obtained from the disturbance energy in figures 3 and 4 complements similar information shown in vorticity plots of figures 6 and 7.

TABLE 1. Leading eigenvalues for the cases

Serial Number	Re = 80 Eigenvalue	Re = 120 Eigenvalue
1.	1.246022	4.599595
2.	0.8018069	3.776959
3.	0.7738014	1.067435
4.	0.3879578	0.9528059
5.	0.1616242	0.8020697
6.	0.1071497	0.7021418
7.	0.1016592	0.5743303
8.	8.0089159e-02	0.5107636
9.	6.1071187e-02	0.3721135
10.	5.8142874e-02	0.3499469
11.	5.3714279e-02	0.3134825
12.	3.7665017e-02	0.2997920

4. Characterizing Vortex shedding and Control by POD

Shed vortices and their control can be attempted if one visualizes them as coherent structures obtained from POD analysis following Sirovich (1987) and Holmes et al. (1996). For handling numerical data over large domain by POD, the *method of snapshots* by Sirovich (1987) is most appropriate, in particular, if the number of input frames or *snapshots*, M is smaller than $(N_x \times N_y)$ - the product of numbers of grid points along the co-ordinate directions. A very brief description of the method follows.

The data obtained by DNS provides the ensemble at M instants in time. If one defines the time varying part of the vorticity field as,

$$\omega'(x,t) = \sum_{m=1}^{M} a_m(t)\phi_m(x) \tag{4.1}$$

Then the eigenvectors ϕ_m's are obtained as the eigenvectors of the covariance matrix whose elements are defined as $R_{ij} = \frac{1}{M}\sum_{m=1}^{M} \omega'(x_i,t_m)\omega'(x_j,t_m)$ with $i,j = 1,2,.....N$ defined over all the collocation points totaling up to N. These complete eigenvectors have eigenvalues that give the probability of their occurrence and their sum giving the total enstrophy of the system. The time variation of eigen-modes can be traced by obtaining $a_m(t)$ from the DNS data by evaluating them from $a_m(t) = \{\omega'(x,t)\phi_m(x)\}$ with the braces denoting the inner-product. The time dependence obtained from the Galerkin expansion of the flow field cannot be used to study absolute instability of the near-wake, as POD is a statistical description of disturbances with respect to an arbitrarily chosen mean field.

In Table-1 the first few leading eigenvalues for $Re = 80$ and $Re = 150$ cases are tabulated that were obtained by taking fifty *snapshots* between $t = 0$ and $t = 49$. For $Re = 80$, first four eigen-modes account for 80% of total energy, while for $Re = 150$ ten modes account for the same. The next 10% energy is contained in another four modes for $Re = 80$ and another ten modes for the higher Reynolds number case. These figures adequately demonstrate the possibility of low-dimensional description of vortex shedding and its control. The cumulative enstrophy content of these modes are shown in the top frame of figure 5.

In figure 5, the time dependent amplitudes of leading eigen-modes are depicted that are obtained from the Galerkin projection of DNS data. Only the first few modes are shown in the figure displaying their time dependence. For both the cases the first two modes account for roughly 50% of the energy, however, the dynamics is different. From figure 2, we have noted periodic variation of lift for $Re = 150$, while it is negligible for $Re = 80$. Any periodic variation of lift is caused due to periodic shedding of vortices in the near-wake. While the onset and growth of vortices are due to an absolute instability, it is their morphosis to convective instability that establishes the vortex street during alternate shedding. It is noted in Deane et al. (1991) and Deane & Mavriplis (1994) that the traveling characteristic (during the transformation from absolute to convective instability) of vortex street is due to coupling of pair of similar amplitude modes that are out of phase by quarter of a period. This is also seen here for $Re = 150$ case where such coupling is seen between a_1 and a_2; and somewhat weaker coupling between a_3 and a_4; a_5 and a_6 and so on. The phase mismatch is not exactly $\pi/2$ for higher modes. For uncontrolled wake cases studied in Deane et al. (1991), the above mentioned coupling between pair of modes was particularly strong. Thus, one can state that the function of the control cylinder is to weaken coupling between successive modes that is responsible for disrupting periodic vortex shedding as compared to uncontrolled case. For $Re = 80$, no such pairing is observed for the leading modes, with weak pairing between a_2 and a_3 only.

There is also a correspondence between the disturbance energy plots of figures 3 and 4 with the $a_i(t)$ plots of figure 5. For example, in figure 4 it is seen that the disturbance energy is least for the frame at $t = 12$ and in figure 5 one notices the corresponding least values for a_1, a_2, a_3 etc. at around the same time. Subsequently at $t = 20$ and 40 the disturbance energy is spread over larger area and so are the $a_i(t)$ for $Re = 80$ case.

The essential difference between these two Reynolds number cases can also be seen in the vorticity contour plots shown in figures 6 and 7 at the indicated times. For both the cases, alternate shedding of vortices are seen in the wake. For $Re = 150$ case, the shedding frequency is significantly higher as compared to the lower Reynolds number case. In figure 3 of Strykowski & Sreenivasan (1990) oscillations of the wake was also seen for $Re = 80$ case. In the present computations also, weak vortices are seen to form at more than 15 diameter behind the main cylinder for this case. It is for this reason, we note that vortex shedding is not completely suppressed even for $Re = 80$. For this case the formation length is significantly higher, so that the loads on the main cylinder is not affected due to the shedding. In contrast, for $Re = 150$ case the formation length is much shorter and the wake-width is also more giving rise to larger drag. This is contrary to what is seen to happen for uncontrolled cases.

The eigenfunctions for both the cases considered are shown in figure 8. For $Re = 80$ only the first three modes are shown in the top three frames. The first leading eigenfunction clearly shows the delay for vortex shedding initiating at the end of elongated structures in the wake. However, the second and third modes show their similarity and the phase difference of $\pi/2$ between them that is responsible for the weakened time periodic behavior of the wake, as also evident from figure 5. The first four eigenfunctions for the $Re = 150$ case have been shown in the bottom four panels of figure 8. In this case, one can clearly see the pairing of the eigenfunctions (similarity)- as also shown in figure 5.

If we compare the information obtained from figures 3 and 4 with the POD modes of figure 8, we note that the effect of control at $Re = 80$ is due to decoupling of the maximum energy-carrying modes. This can also be interpreted as due to the quenching of unsteady effects due to the effects of an oncoming shear flow at relatively lower Reynolds number globally- as shown in figure 4. However, for $Re = 150$ the control cylinder is at a relatively higher Reynolds number that while weakening the coupling of the POD modes of figure 8, does not have global damping of unsteadiness as seen for $Re = 80$ case. This is also clearly evident from figure 3 for the disturbance energy plots. Such effects of shear flow past control cylinder also qualitatively changes the drag behavior with Reynolds number, as compared to uncontrolled cases.

5. Summary

The results of a theoretical study are reported here for the alteration of vortex shedding pattern in the wake of a cylinder at low Reynolds numbers (80 and 150) by a control cylinder placed in the near wake. The numerical results have been obtained by using a accurate over-set-grid method developed here. For the identical location of the control cylinder, for the lower Reynolds number vortex shedding is delayed spatially, with loads on the main cylinder not showing strong periodic variation. However, for $Re = 150$ case, vortex shedding is mildly altered. The effect of the control cylinder is explained by using the receptivity equation (1.1) developed in Sengupta et al. (2003). It is seen that the control cylinder is responsible for creating different effects at the two Reynolds numbers. This is due to the fact that the effective Reynolds number for the control cylinder is small for both the cases (11.4 and 21.4), when Re increases from 80 to 150. Also, the effects of shear of the oncoming flow at such lower Reynolds numbers have significantly different magnitude. The DNS data are also analyzed using the POD technique of Holmes et al. (1996) and Sirovich (1987) to explain the function of the control cylinder. It is seen that the control cylinder prevents the pairwise coupling of the eigen-modes that are seen to be responsible for vortex shedding phenomenon- that has been demonstrated in Deane et al. (1991) and Deane & Mavriplis (1994). For the present cases, it is seen that this coupling is disrupted strongly for $Re = 80$ and rather weakly for $Re = 150$. However, the presence of the control cylinder has the effect of narrowing down the wake in comparison to uncontrolled case.

The global effects of shear flow past the control cylinder at very small Reynolds number has its effect on the vortex shedding from the main cylinder as can also be interpreted in terms of disturbance energy variation via equation (1.1). These are shown in figures 3 and 4 for the two Reynolds number cases. This approach provides a complementary picture to that obtained from POD analysis.

REFERENCES

Chesshire, G, & Henshaw, W.D. 1990 Composite overlapping meshes for the solution of partial differential equations. *J. Comput. Phys.* **90**, 1–64.

Deane, A.E., Kevrekidis, I.G., Karniadakis, G.E. & Orszag, S.A. 1991 Low-dimensional models for complex geometry flows: Application to grooved channels and circular cylinders. *Phys. Fluids A* **3(10)**, 2337–2354.

Deane, A.E. & Mavriplis, C. 1994 Low-dimensional description of the dynamics in separated flow past thick airfoils. *AIAA J.* **32(6)**, 1222–1227.

Henshaw, W.D. 1994 A fourth order accurate method for the incompressible Navier-Stokes equations on overlapping grids. *J. Comput. Phys.* **113(1)**, 13–25.

Holmes, P., Lumley, J.L. & Berkooz, G. 1996 *Turbulence, Coherent Structures, Dynamical Systems and Symmetry.* Cambridge University Press, U.K.

Jackson, C.P. 1987 A finite element study of the onset of vortex shedding in flow past variously shaped bodies. *J. Fluid Mech.* **182**, 23–45.

Nair, M.T. & Sengupta, T.K. 1996 Onset of asymmetry: Flow past circular and elliptic cylinders. *Int. J. Num. Meth. Fluids* **23**, 1327–1345.

SENGUPTA, T.K. 2004 *Fundamentals of Computational Fluid Dynamics.* Universities Press, Hyderabad, India

SENGUPTA, T.K., DE, S. & SARKAR, S. 2003 Vortex-induced instability of an incompressible wall-bounded shear layer. *J. Fluid Mech.* **493**, 277–286.

SENGUPTA, T.K., GANERIWAL, G.& DE, S. 2003a Analysis of central and upwind compact schemes. *J. Comput. Phys.* **192**, 677-694.

SENGUPTA, T.K., KASLIWAL, A., DE, S. & NAIR, M. 2003b Temporal flow instability for Magnus-Robins effect at high rotation rates. *J. Fluids Struct.* **17** (7), 941–953.

SENGUPTA, T.K. & DIPANKAR, A. 2005 Subcritical instability on the attachment-line of an infinite swept wing. *J. Fluid Mech.* **529**, 147–171.

SENGUPTA, T.K., SIRCAR, S.K. & DIPANKAR, A. 2005 High accuracy schemes for DNS and acoustics. *J. Sci. Comput.* **25** (2), 1–43.

SENGUPTA, T.K., VIKAS, V. & JOHRI, A. 2005a An improved method for calculating flow past flapping and hovering airfoils. *Theo. Comput. Fluid Dyn.* (Paper accepted for publication)

SIROVICH, S. 1987 Turbulence and the dynamics of coherent structures. Part I,II and III. *Q. Appl. Maths.* **45**, 561–590.

STEGER, J.L. & BENEK, J.A. 1987 On the use of composite grid schemes in computational aerodynamics. *Comp. Methods Appl. Mech. Engg.* **64**, 301–320.

STRYKOWSKI, P.J. 1986 *T*he Control of Absolutely and Convectively Unstable Shear Flows. Ph. D. dissertation, Yale University.

STRYKOWSKI, P.J. & SREENIVASAN, K.R. 1990 On the formation and suppression of vortex 'shedding' at low Reynolds numbers. *J. Fluid Mech.* **218**, 74–107.

Appendix- A

Dispersion Relation Preservation Properties of Numerical Schemes

The requirements for DNS of physically unstable flows are related to stability and dispersion relation preservation (DRP) properties. To study these properties we consider the propagation of wave-packet to be governed by the linear convection equation,

$$\frac{\partial u}{\partial t} + c\frac{\partial u}{\partial x} = 0 \qquad c > 0 \tag{A.1}$$

where c is the phase speed and this equation represents non-dispersive wave propagation i.e. the initial wave form retains its shape without physical dispersion. we examine the $OUCS3$ spatial scheme that has been used here for computing the flow in the multiply-connected domain for its numerical stability and DRP property vis-à-vis the second order central differencing scheme. For both the methods, four-stage Runge-Kutta time integration scheme has been used.

To provide a consistent comparison, equation (A.1) is solved here as the exact solution and numerical properties of it are well known. For the central differencing scheme the spatial derivative is calculated from

$$u_i' = \frac{u_{i+1} - u_{i-1}}{2h} \tag{A.2}$$

For the $OUCS3$ scheme the spatial derivatives are calculated implicitly by solving the following set of equations,

$$u_1' = \frac{1}{2h}\left(-3u_1 + 4u_2 - u_3\right) \tag{A.3}$$

$$u_2' = \frac{1}{h}\left[\left(\frac{2\alpha_2}{3} - \frac{1}{3}\right)u_1 - \left(\frac{8\alpha_2}{3} + \frac{1}{2}\right)u_2 + (4\alpha_2 + 1)u_3 - \left(\frac{8\alpha_2}{3} + \frac{1}{6}\right)u_4 + \frac{2\alpha_2}{3}u_5\right] \quad (A.4)$$

$$for j = 3\ \ to\ \ (N-2): \qquad \beta_{j-1}u'_{j-1} + u'_j + \beta_{j+1}u'_{j+1} = \frac{1}{h}\sum_{k=-2}^{k=2} q_k u_k \quad (A.5)$$

$$u'_{N-1} = -\frac{1}{h}\left[\left(\frac{2\alpha_{N-1}}{3} - \frac{1}{3}\right)u_1 - \left(\frac{8\alpha_{N-1}}{3} + \frac{1}{2}\right)u_2 + \right.$$
$$\left.(4\alpha_{N-1} + 1)u_3 - \left(\frac{8\alpha_{N-1}}{3} + \frac{1}{6}\right)u_4 + \frac{2\alpha_{N-1}}{3}u_5\right] \quad (A.6)$$

$$u'_N = -\frac{1}{2h}\left(-3u_N + 4u_{N-1} - u_{N-2}\right) \quad (A.7)$$

where $\beta j \pm 1 = 0.3793894912 \pm \eta/60, q_{\pm 2} = 0.1832051925/4 + \eta/300, q_{\pm 1} = 1.57557379/2 + \eta/30$ and $q_0 = -11\eta/150$ with $\eta = 0$;These coefficients and additional ones are as given in Sengupta *et al.* (2003a).

The linear algebraic equations (A.3) to (A.7) can also be alternately written as,

$$\frac{\partial u_j}{\partial x} = \frac{1}{h}\sum_{l=1}^{N} C_{lj} u_j e^{ik(x_l - x_j)} \quad (A.8)$$

For the time integration of (A.1) and other convection dominated flow problems, the four stage Runge- Kutta method (RK_4) provides best numerical properties as described below. If we denote, $L(u) = -c\frac{\partial u}{\partial x}$, then the following sub-steps are used in RK_4 to advance the variable from $u^{(n)}$ to $u^{(n+1)}$,

$$Step - 1: \qquad u^{(1)} = u^{(n)} + \frac{\Delta t}{2}L[u^{(n)}]$$

$$Step - 2: \qquad u^{(2)} = u^{(n)} + \frac{\Delta t}{2}L[u^{(1)}]$$

$$Step - 3: \qquad u^{(3)} = u^{(n)} + \frac{\Delta t}{2}L[u^{(2)}]$$

$$Step - 4: \qquad u^{(n+1)} = u^{(n)} + \frac{\Delta t}{6}\left(L[u^{(n)}] + 2L[u^{(1)}] + 2L[u^{(2)}] + L[u^{(3)}]\right)$$

It is straightforward to show that the numerical amplification factor for RK_4 scheme for the j^{th} node for a wave number k is given by (see Sengupta *et al.* (2005) for details),

$$G_j(kh, N_c) = 1 - A_j + \frac{A_j^2}{2} - \frac{A_j^3}{6} + \frac{A_j^4}{24} \quad (A.9)$$

where $A_j = N_c \sum_{l=1}^{N} C_{jl} e^{ikx_l - x_j}$ and N_c is the CFL number defined as $\frac{c\Delta t}{h}$. If we represent the amplification factor in terms of its real and imaginary part as, $G(kh, N_c) = G_r + iG_i$, then the numerical group velocity is given by (see Sengupta *et al.* (2005))

$$\frac{V_{gN}(k)}{c} = \frac{1}{N_c h}\frac{d\gamma}{dk} \quad (A.10)$$

where $tan\gamma = -\frac{G_i}{G_r}$. Using (A.2) in (A.8), one can obtain the expression for G_j and V_{gN}/c from (A.9) and (A.10) for the second order central difference scheme.

In figure 9, the numerical amplification rate and group velocities are compared between $OUCS3$ and $CD2$ schemes. It is readily evident that both the schemes have a small range of N_c for which one has the desired neutral numerical stability- with $CD2$ scheme having a larger range. It would therefore appear that $CD2$ scheme is better on account of this property. However, the numerical group velocity property of the two schemes are quite different. We have marked the regions for these two schemes where the numerical group velocity departs from the physical group velocity by less than equal to 1% error and on this tolerance limit $CD2$ has a very small admissible range of kh for the full range of displayed N_c. In contrast, $OUCS3$ has a significant large range of kh and N_c, where DRP property is acceptable. We also note that for both the schemes there is a limiting value of kh above which the numerical group velocity is negative as marked in the figures i.e. the computed signal would travel in the wrong direction. For $OUCS3$ scheme, this limiting value is above 2.4 while for the $CD2$ scheme this is lower than 1.6.

To show the implication of the results shown in figure 9, we compute the propagation of a wave packet as governed by (A.1) with $c = 1$. We consider the following initial wave packet given by,

$$u(x,0) = e^{-16(x-3/2)^2} sin k_0 x \qquad (A.11)$$

with $k_0 = 1.7/h$, such that the $CD2$ scheme will show this wave packet to travel in the negative x- direction while the $OUCS3$ scheme will have correct propagation direction and speed of propagation. In figure 10, computed results are shown for the $CD2$ scheme, along with the exact solution at each time instants, shown by dotted line. It is clearly seen that the wave packet amplitude is maintained correctly, but it travels in the wrong direction. In figure 11, computed results are for the $OUCS3$ scheme and in this case the computed signal and the exact signal overlaps on each other. This example clearly demonstrates the fact that for computing unstable flows, one must choose a scheme that preserves DRP property.

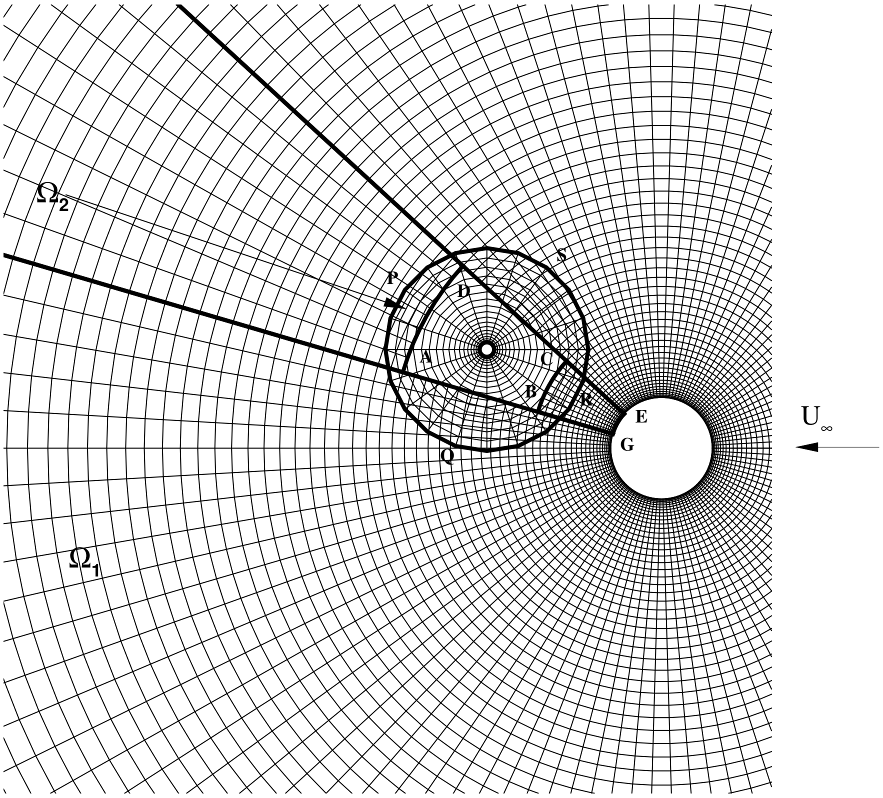

FIGURE 1. Over-set-grid used for the presented numerical results. Only some representative grid-lines are shown. The diameter of the control cylinder is $1/7^{th}$ of D and Ω_2 extends up to D only.

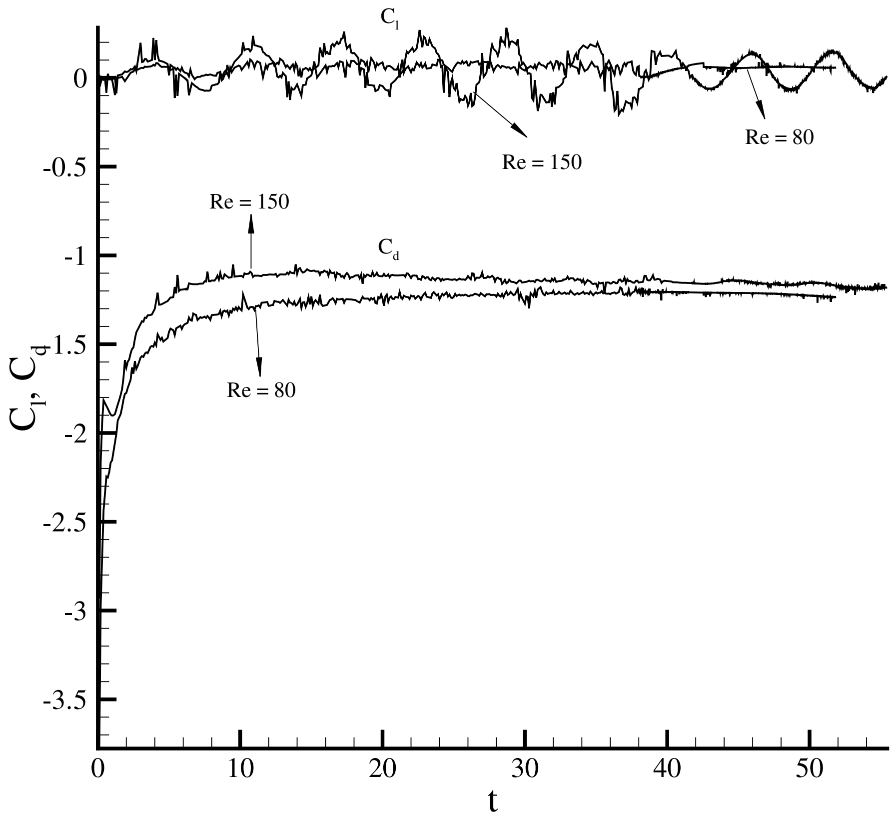

FIGURE 2. Lift and drag coefficients shown as function of time for $Re = 80$ and 150 cases.

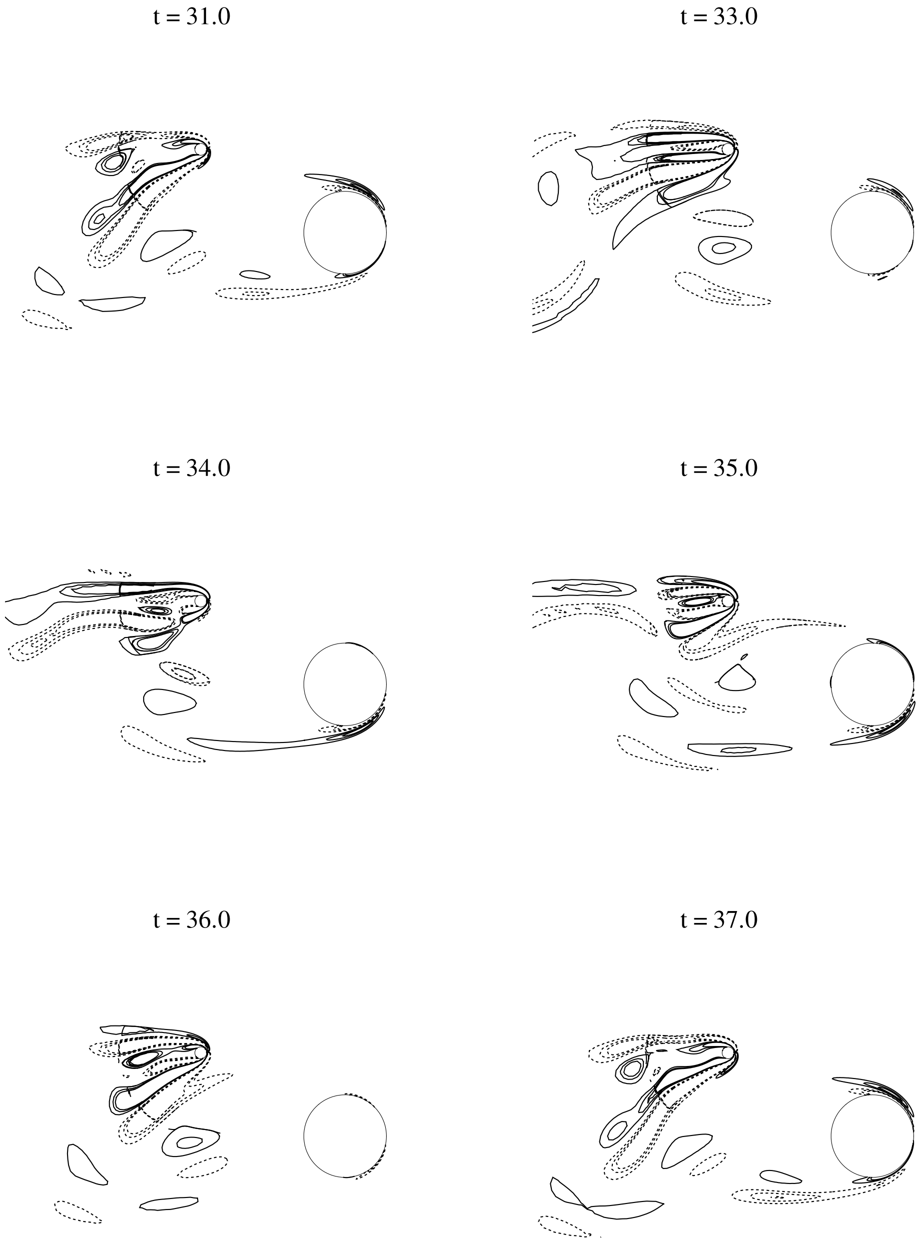

FIGURE 3. Contours of the right hand side of disturbance energy equation (1.1), for Re = 150. The dotted line corresponds to energy sources and solid lines represent sinks.

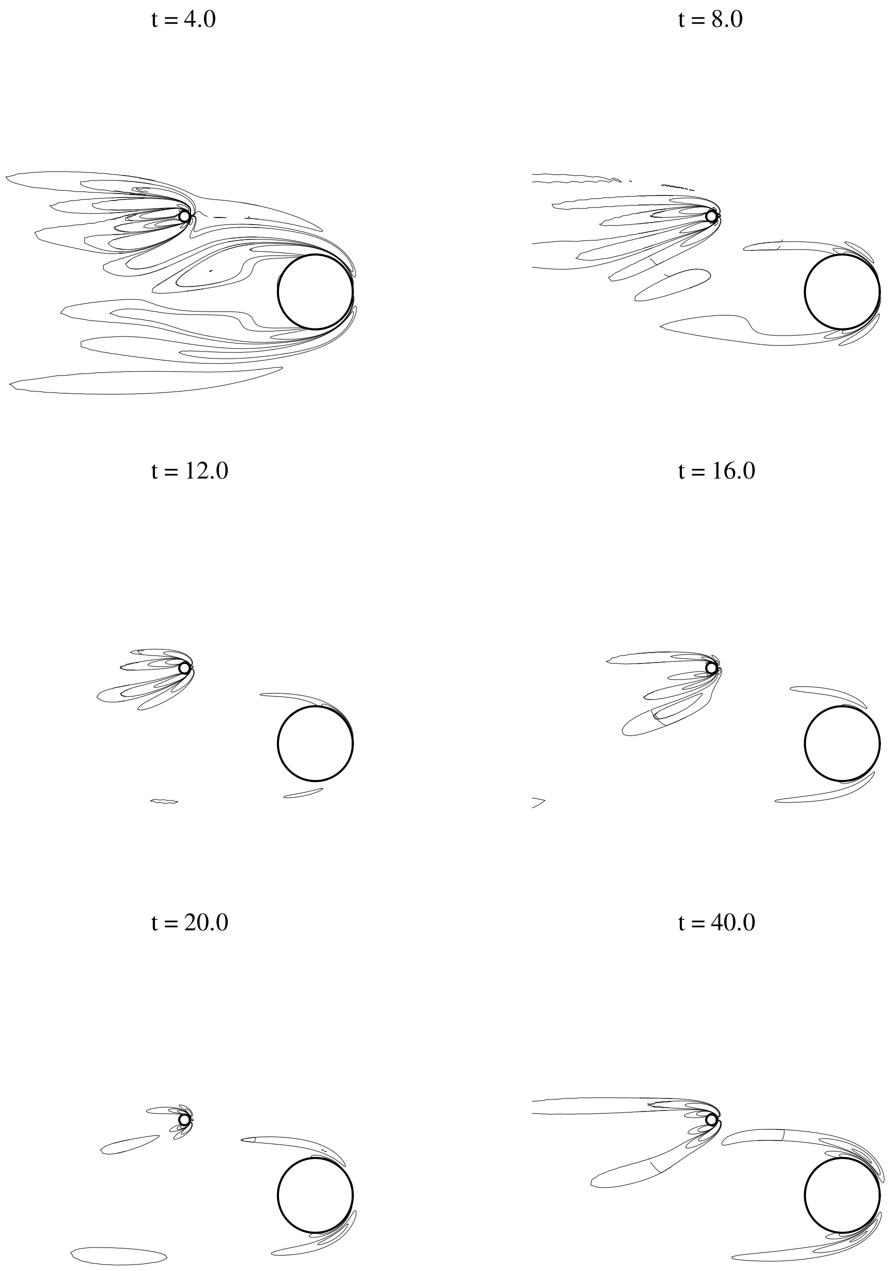

FIGURE 4. Contours of the right hand side of disturbance energy equation (1.1), for Re = 80. The dotted line corresponds to energy sources and solid lines represent sinks.

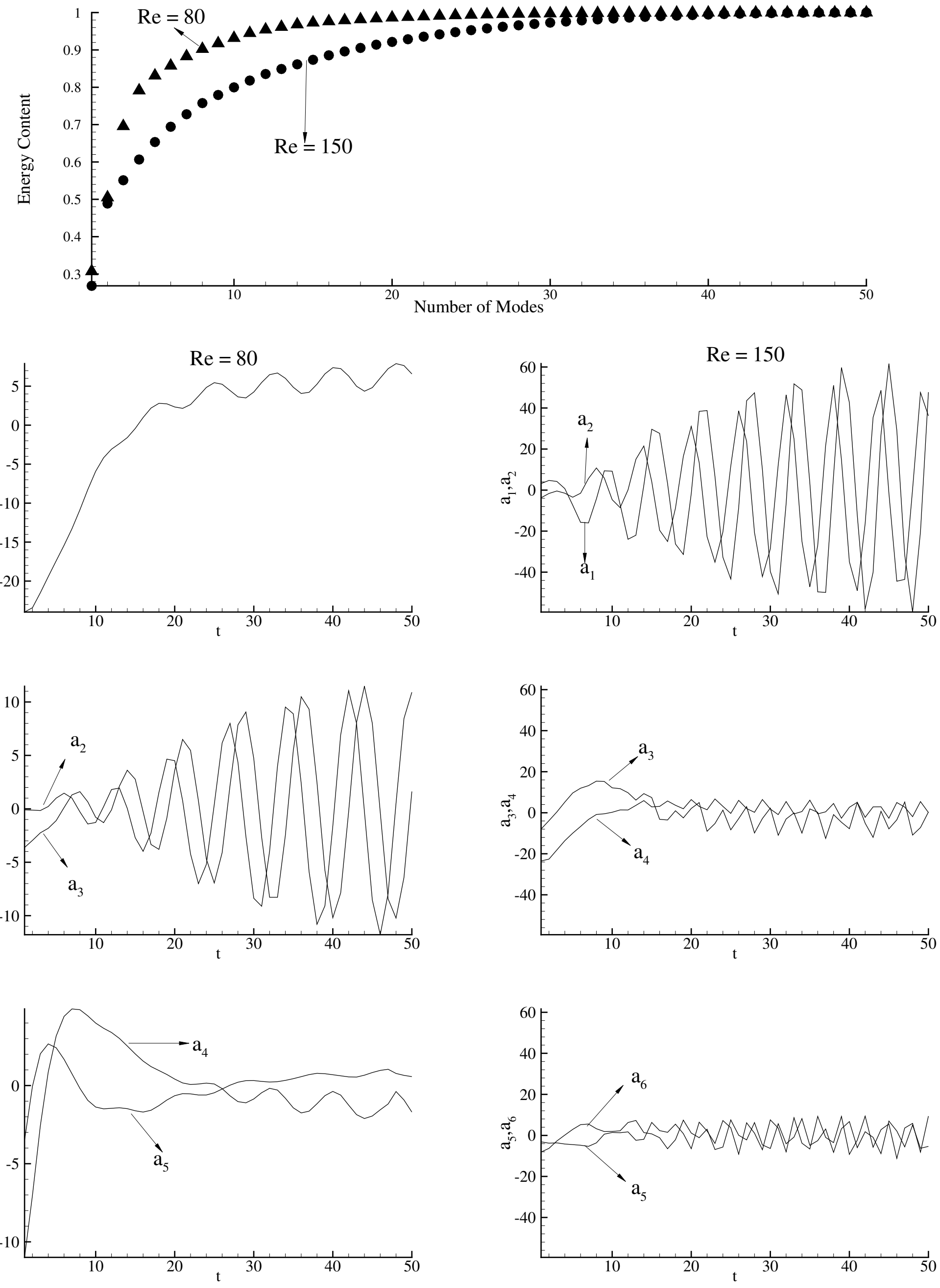

FIGURE 5. Proper orthogonal decomposition of the DNS data. Top frame shows the cumulative energy content of different modes. Bottom six panels show the time variation of the amplitude of the eigenfunctions.

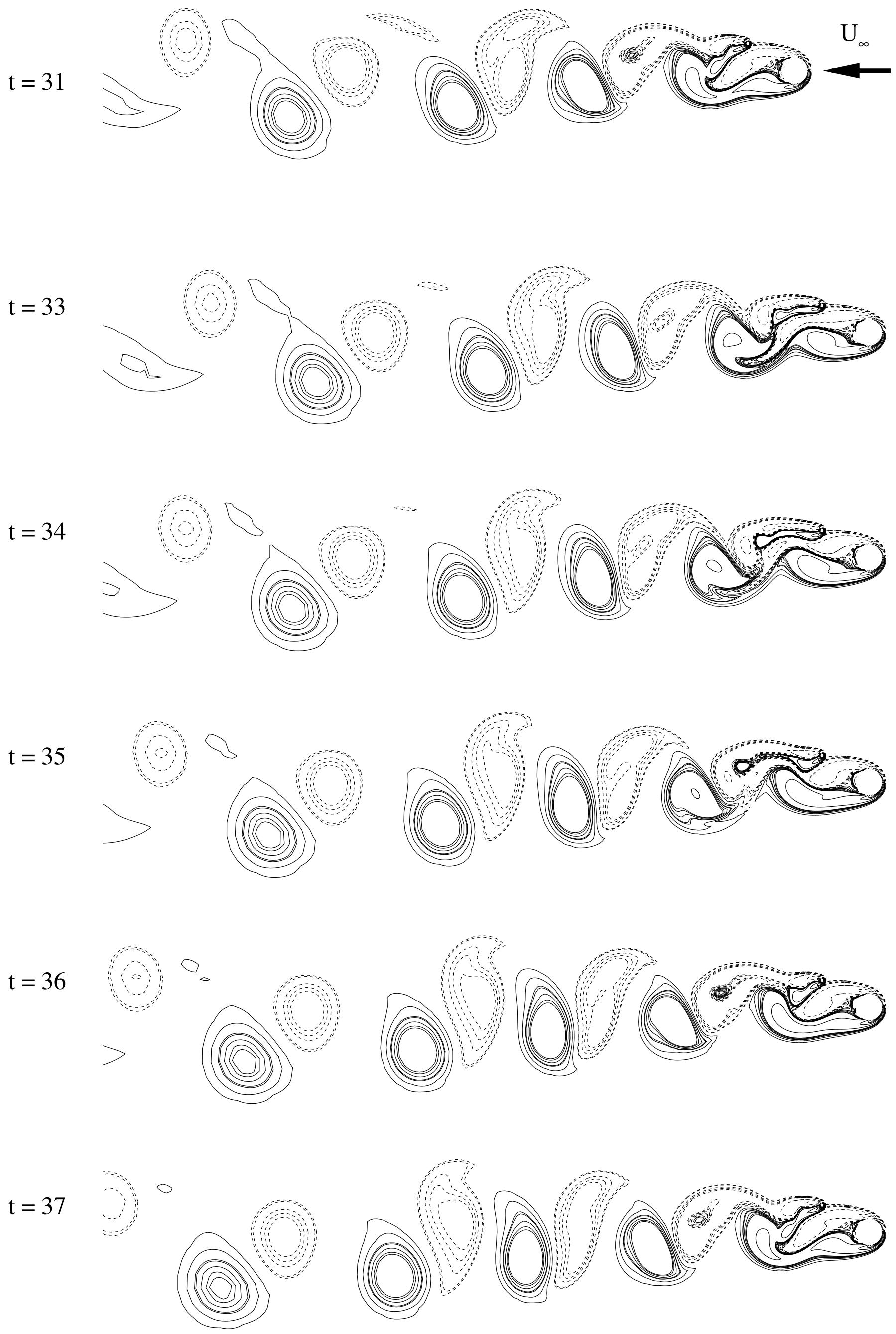

FIGURE 6. Vorticity contours are shown at the indicated times, for Re = 150 case. Negative vorticity is shown by dashed line.

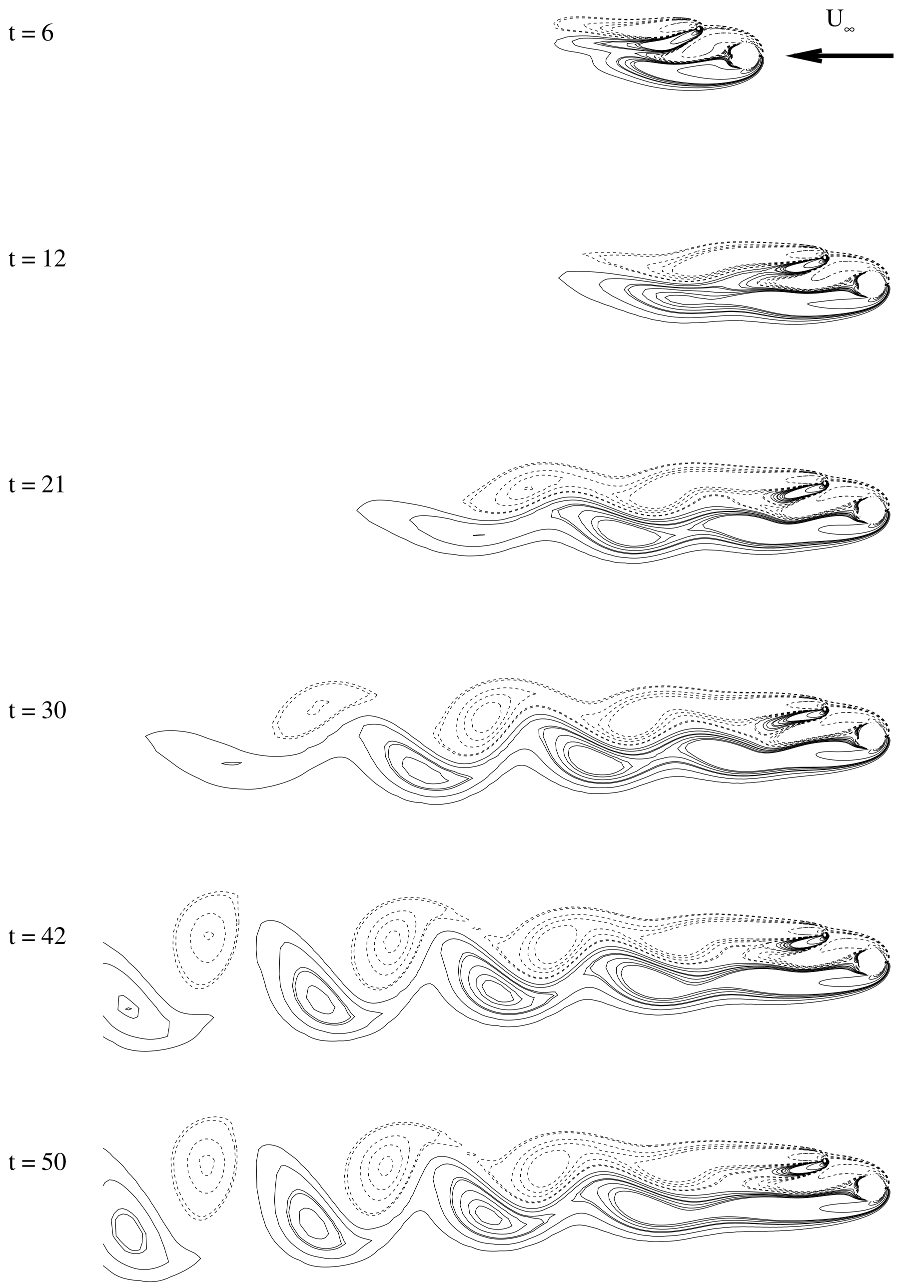

FIGURE 7. Vorticity contours are shown at the indicated times, for Re = 80 case. Negative vorticity is shown by dashed line.

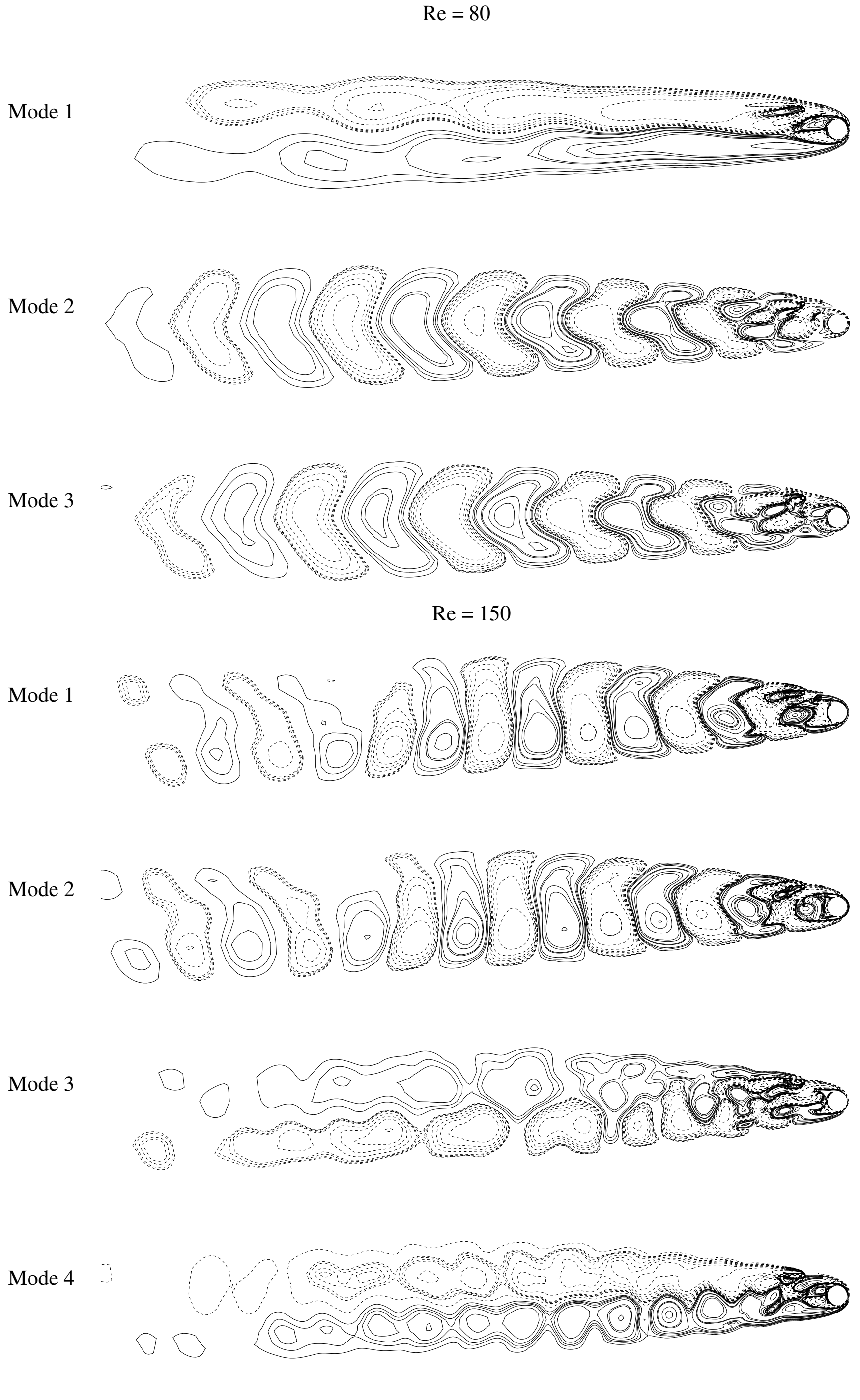

FIGURE 8. Eigenfunction plots for the Re =80 (top) and Re = 150 (bottom) cases.

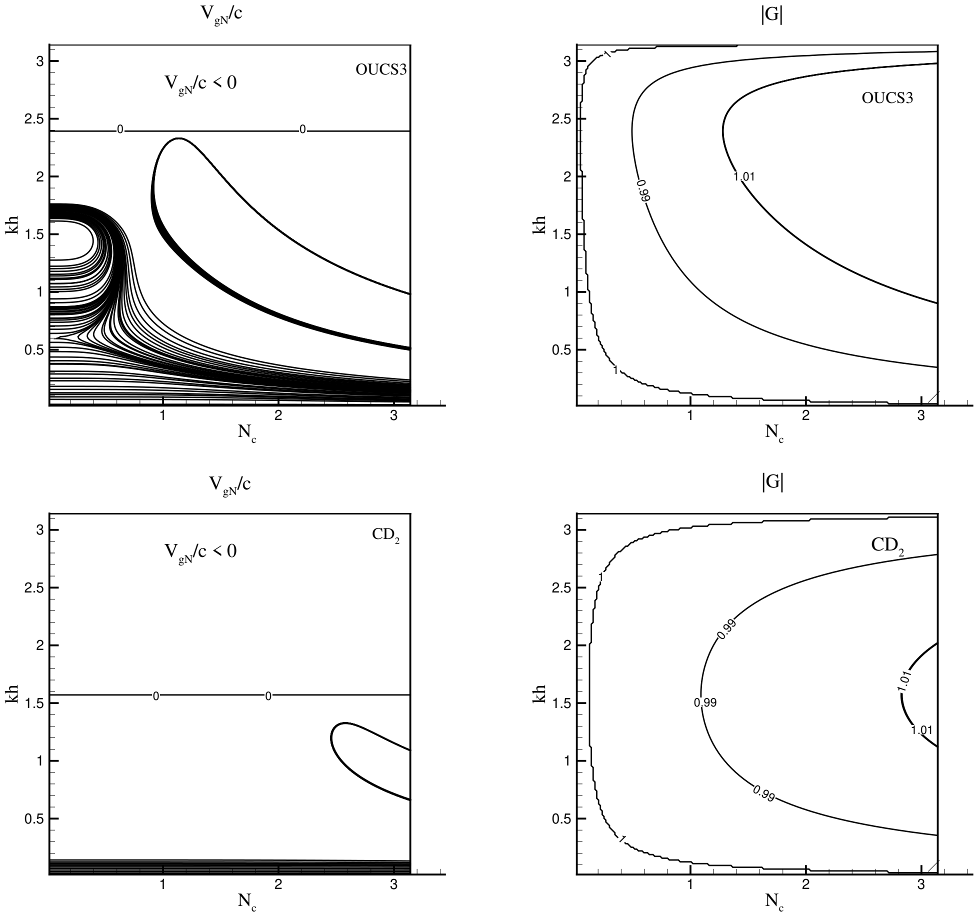

FIGURE 9. Contours showing Scaled numerical group velocity (V_{gN}/c) and Amplification factor ($|G|$) for 1D wave equation using $OUCS3$ and CD_2 spatial discretization schemes and RK_4 time marching scheme.

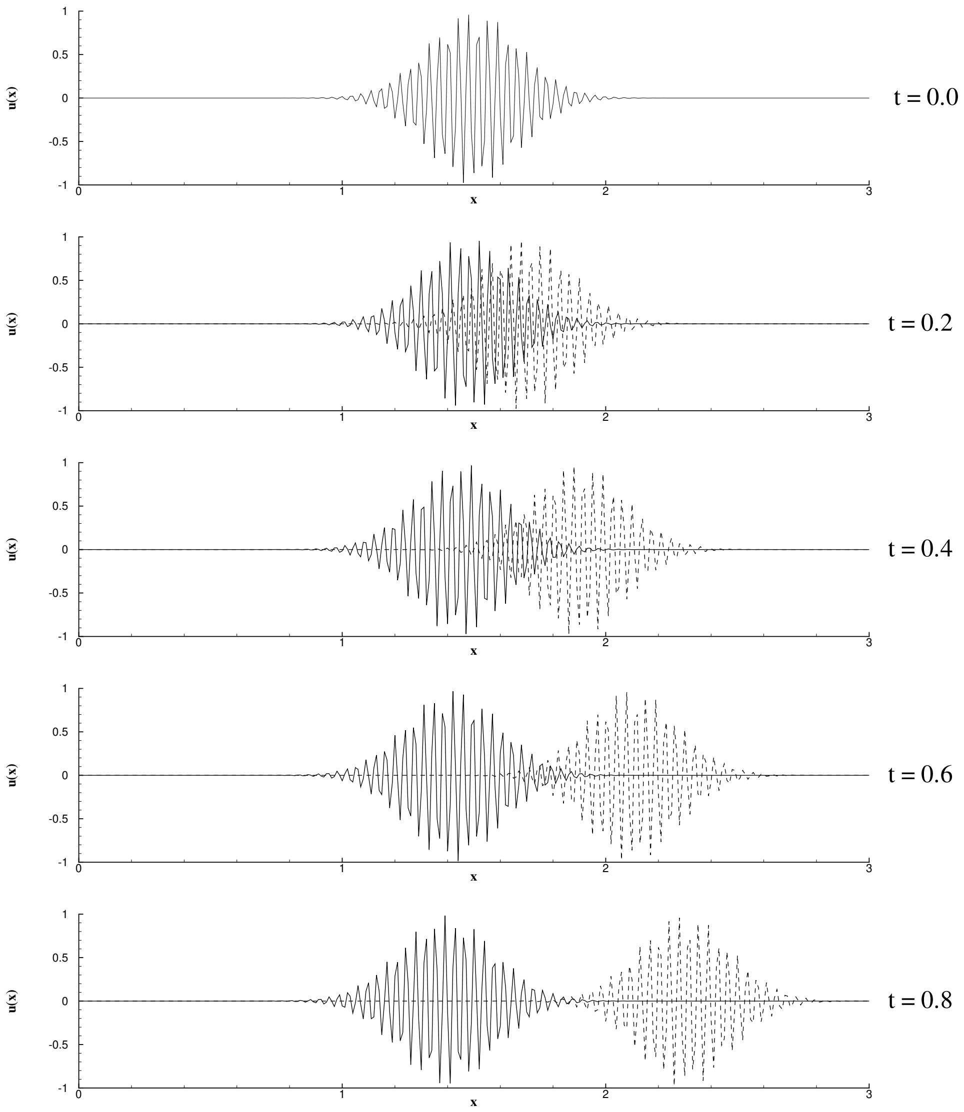

FIGURE 10. Computed solution (solid line) of Eq. (A.1) is shown using (A.11) as the initial condition for $k = 1.7/h$, using CD_2 for spatial discretization. Analytical solution to the same is shown by dashed line.

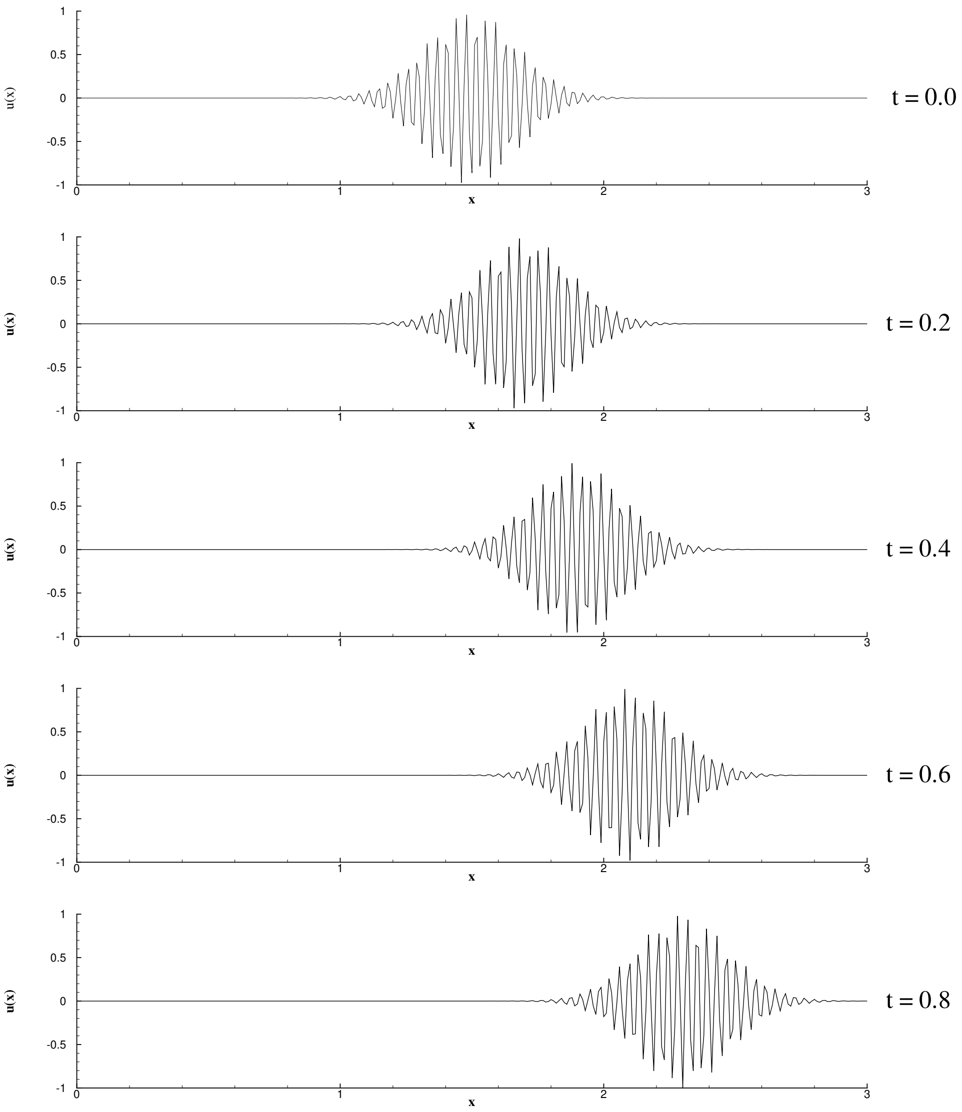

FIGURE 11. Computed solution of Eq. (A.1) is shown using (A.11) as the initial condition for $k = 1.7/h$, using $OUCS3$ for spatial discretization.